ACS OMEGA

http://pubs.acs.org/journal/acsodf

Article

Change Laws of Pore–Fracture Structure of Coal under High-Temperature Steam Shock

Youping Xu, Baiquan Lin,* and Yuxue Li

Cite This: *ACS Omega* 2022, 7, 44298–44309

Read Online

ACCESS | Metrics & More | Article Recommendations

ABSTRACT: Injecting steam into coal seam is an important means to accelerate gas desorption and improve gas extraction efficiency. However, the change law of pore–fracture structures of coal after high-temperature steam shock (thermal shock) is still unclear. Through this study, pore–fracture structures of coal samples before and after thermal shock were compared and analyzed based on the experimental methods of surface pore and fracture extraction, scanning electron microscopy (SEM), and nuclear magnetic resonance (NMR) spectroscopy. The results show that after thermal shock, the surface porosity, max equivalent fracture width, fracture lengths, fracture number, and probability entropy of coal samples increased significantly, and the increment of bituminous coal was greater than that of anthracite. This indicates that thermal shock can promote the development of coal pores, which is significantly better for bituminous coal than anthracite. A SEM analysis reveals that fractures tend to appear at the interface between minerals and coal matrix. The NMR analysis demonstrates that the absolute increment of micropores is the largest, followed by that of mesopores, and that of macropores is the smallest. The increase of porosity in coal shows pore enlargement and penetration, which enhance the connectivity between the pores, thus providing a smoother channel for methane migration. Heterogeneous distribution of mineral components with different thermal expansion coefficients as well as the temperature gradient is the fundamental mechanism behind thermal stress-induced porosity development. The research results provide theoretical support for enhanced gas extraction technology by high-temperature steam injection into coal seams.

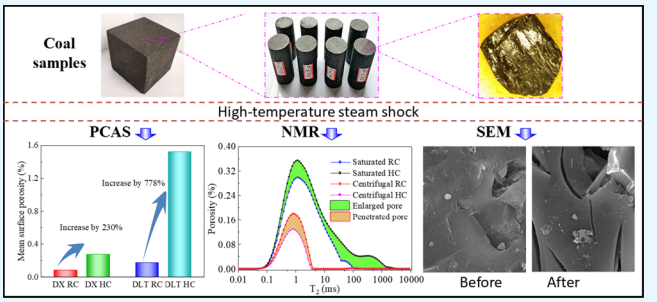

1. INTRODUCTION

Coal is the pillar energy in China whose coal consumption accounted for 56% of the total energy consumption in 2021. As China commits to the world to achieve carbon peak in 2030 and carbon neutralization in 2060, the proportion of China's coal consumption in the total one-time energy consumption will decline year by year, which makes it urgent to find low-carbon energy for substitution. Coalbed methane (CBM), a kind of coal-associated clean energy with abundant reserves and broad development prospects, is an important carrier to promote the revolution of energy production and consumption.[1,2]

Coal is a heterogeneous and natural porous medium with a complex internal structure. Most CBM is stored in the coal seam through adsorption. As the pore–fracture network structure inside the coal is the main channel for gas seepage, the permeability of the coal seam is the key factor that determines the effect of CBM extraction. With the depletion of shallow resources, coal mining continues into the deeper part with increasing CBM reserves and pressure and gradually decreasing permeability of the coal reservoir.[3,4] Therefore, increasing the permeability of coal seams is a major challenge for CBM development and efficient gas extraction. Hydraulic fracturing is a widely used measure to promote CBM production currently. The commonly used hydraulic fracturing has some deficiencies such as serious fracturing fluid filtration, low flowback rate, short and complex fracturing fractures, excessive consumption of water resources, and water lock effect affecting CBM extraction.[5−9] In order to increase the permeability of coal seams and improve the CBM extraction effect, in view of the temperature-sensitive characteristics of gas adsorbed coal,[10] many scholars at home and abroad have begun to explore and develop new technologies to improve the permeability by adopting heat injection to shock the coal in recent years[11,12] so as to accelerate the desorption of adsorbed gas and change the pore–fracture structure of raw coal and then enhance the permeability and production.

With respect to heat injection into the coal seams, relevant scholars have put forward various technical schemes, including

Received: September 8, 2022
Accepted: October 27, 2022
Published: November 17, 2022

microwave heating coal,[13] gas heating coal,[14−16] and steam/hot water heating coal,[17] according to different working media. Based on these technical schemes, basic research studies have been carried out, achieving some results. Based on the heating function of microwave, some scholars have studied the characteristics of temperature change, evolution law, and mechanism of pore structure of coal samples under microwave irradiation.[18−22] These studies have promoted the progress of this technology, but they are all based on small size coal samples. How to apply this technology under the condition of a large coal field size is a key difficulty. Although some scholars have put forward application ideas,[23] no successful application cases have been reported. Salmachi used hot water (80 °C) for coal seam heat injection, increasing the temperature of coal seam by 30 °C. As a result, the CBM recovery ratio increased by about 60% and the extraction rate increased by about seven times.[24] Wang et al. studied the permeability change and increase mechanisms of coal under the cyclic temperature and found that the heterogeneity of coal and thermal stress are the main internal mechanisms of permeability increase under high-temperature shock.[25] Shahtalebi et al. found that thermal excitation could effectively raise the diffusion rate of gas in a coal matrix through experiments and numerical simulations.[26] Cai et al. confirmed that high-temperature pyrolysis of coal (>400 °C) could induce the loss of oxygen-containing functional groups and minerals, resulting in increasing seepage pores and fractures.[27] Teng et al. concluded that gas pyrolysis, heat removal of water and volatile matter content, and thermal fracture of matrix are the main factors accounting for increasing coal porosity and permeability.[28] In addition, injecting heat into the coal seam can effectively increase the production of CBM.

The above research studies have made some contributions to heat injection in coal seam to improve gas extraction and deepen the understanding of physical and chemical properties of coal heated in different ways. However, there are few studies on the change rule of the coal pore morphology and the thermal mechanism of high-temperature steam shock on coal. Therefore, it is of prime significance to study the evolution law of coal pores and fractures after injecting high-temperature steam into coal.

2. EXPERIMENTAL FACILITY AND MATERIALS

In order to study the evolution law of pore−fracture structure of coal subject to high-temperature steam shock, an experimental platform was developed, and two kinds of coal samples with different metamorphic degrees were selected. After machine shaping, the macroscopic fractures and microscopic pores of coal samples before and after thermal shock were studied, respectively. In terms of macroscopic fractures, photographs of the coal sample surfaces before and after thermal shock were collected, and fractures were extracted and analyzed with the Particles (Pores) And Cracks Analysis System (PCAS). In terms of microscopic pores, the coal samples were tested before and after thermal shock based on the nuclear magnetic resonance (NMR) test method, and the evolution law of the coal pore−fracture structure was analyzed.

2.1. Coal Samples. Coal samples from Shanxi Daxi coal mine (DX) and Shaanxi Daliuta coal mine (DLT) were processed into cylinders of 25 mm in diameter and 50 mm in length and cubes of 100 mm in length (Figure 2). The proximate analysis and vitrinite reflectance of samples in Table 1 reveal that DX coal is high metamorphic anthracite and DLT coal is a low-rank bituminous coal, which meet the requirements of selecting coals with different metamorphic degrees.

Table 1. Proximate Analysis and Vitrinite Reflectance Results of DX and DLT Coals[a]

	proximate analysis (%)					
coal sample	M_{ad}	A_{ad}	V_{daf}	FC_d	$R_{0,max}$ (%)	coal rank
DX	1.40	7.40	8.96	84.30	2.98	anthracite
DTL	9.24	3.04	35.83	62.22	0.56	bituminous

[a] M_{ad}, moisture content (air-dried basis); A_{ad}, ash content (air-dried basis); V_{daf}, volatile matter content (dried and ash-free basis); FC_d, fixed carbon content (dried basis); and $R_{0,max}$, maximum vitrinite.

2.2. Experimental Facility. The experimental equipment mainly includes a steam shock coal experimental platform, and the testing equipment mainly includes a high-definition camera, an electron microscope, and a NMR spectrometer. The fracture extraction is performed with the help of PCAS software.

(1) Steam shock coal experimental platform. The self-built experimental platform consists of two major parts: a high-temperature steam generation system and an autoclave (Figure 1).

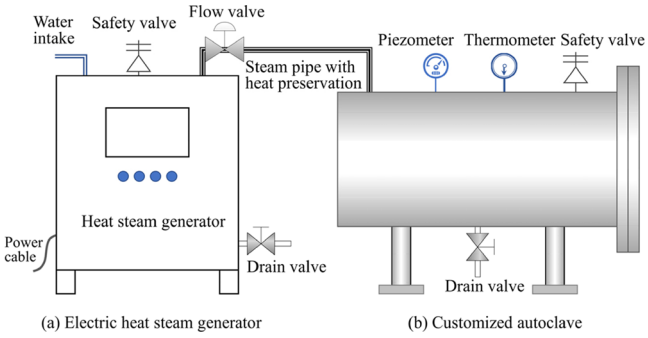

Figure 1. Steam heating experimental platform. (a) Electric heat steam generator; (b) customized autoclave.

1. High-temperature steam generation system: As shown in Figure 1a, the main function of this system is to produce high-temperature steam for the autoclave. The high-temperature steam generator, which has a working pressure of 3 MPa, can use deionized water to produce superheated steam of 300 °C (internal temperature of the steam generator).
2. Customized autoclave: As shown in Figure 1b, it is mainly used to provide a container with good thermal insulation performance for heating coal. Its maximum working pressure is 1.65 MPa, beyond which the top safety valve will get started. There is a drain valve at the bottom. After testing, the maximum temperature when the steam generator reaches the autoclave is about 210 °C.

(2) PCAS: In the experiment of macroscopic crack extraction, images of samples are processed by PCAS software, professional software used to quantify the pore system and the crack system in images. The software can be used to automatically identify various pores and fractures and obtain geometric and statistical parameters. Compared with traditional manual measurement methods, the PCAS system boasts simplicity, efficiency, and repeatability.

(3) SEM: SEM characterization was completed in the Modern Analysis and Computing Center of China

https://doi.org/10.1021/acsomega.2c05849
ACS Omega 2022, 7, 44298−44309

University of Mining and Technology using a ZEISS SIGMA field-emission SEM of Germany. The resolution of the secondary electron image is 4 nm and the magnification is 12∼1,000,000.

(4) NMR: The MINI MR NMR pore structure analyzer is used for comparing the experimental results of microscopic pores and fractures. The analyzer uses a permanent magnet with a magnetic field intensity being 0.53 T. In the test, the temperature of the permanent magnet is 32 °C, the echo interval is 0.225 ms, the scanning times are 16, and the sampling frequency is 333.333 KHz. After the test, the T_2 relaxation distribution is calculated with the joint iterative reconstruction technique, and the number of iterations is 1×10^4.

The principle of the NMR test is that some atomic nuclei have net magnetic distance and angular momentum, and when there is an external magnetic field, the atomic nuclei will respond to the magnetic field and produce a measurable signal.[29] For the atomic nuclei found in most strata, the signal caused by the external magnetic field is weak, and only hydrogen nuclei can produce a strong signal. So far, almost all NMR rock tests are based on the response of hydrogen nuclei. According to many researchers, NMR can effectively measure the pore distribution of coal for two reasons: (1) only a few mineral components in coal are magnetic and (2) when the test frequency is low enough, the signal generated by the hydrogen nucleus in the solid cannot be measured.[30,31] Therefore, NMR can be used to effectively test the pore structure in coal.

2.3. Experimental Scheme. Changes of surface and internal pores and fractures of the coal samples before and after high-temperature steam shock are compared in the experiment, and the experimental scheme is shown in Figure 2. During the experiment, the indoor temperature is 26 °C. The

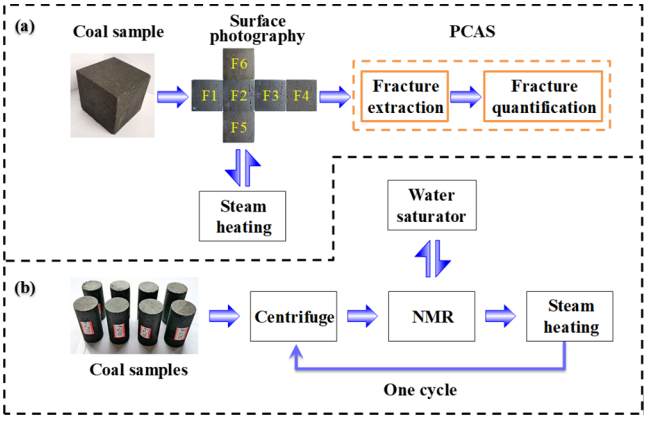

Figure 2. Macroscopic and microscopic pore−fracture experiments. (a) Steps of the macroscopic pore−fracture experiment. (b) Steps of the microscopic pore−fracture experiment.

external pore−fracture structure experiment is shown in Figure 2a, and the steps are described as follows:

(1) Select one cubic DX and DLT raw coal with a side length of 10 cm and take photos of six faces of each coal sample with high-definition camera, which are numbered F1−F6 in turn.

(2) Put the abovementioned samples into the steam heating experimental platform and adjust the temperature of the steam generator panel to 300 °C. Once the autoclave achieves heat balance, the temperature shown on the gauge is 203 °C and the pressure shown on the pressure gauge is 1.65 MPa. Stop heating after 180 min, and take out the coal samples after exhausting and depressurizing the autoclave.

(3) Take pictures of six faces of the coal samples again.

(4) Expand the photos in the shape of a cube as shown in surface photography in Figure 2a. Then extract the crack with PCAS software and quantitatively characterize the characteristics of the crack.

The experimental procedure of SEM is similar to that of a high-definition camera, and the difference is that the shooting object is a block coal sample with a side length of about 1 cm.

The steps of the internal pore−fracture structure experiment are described as follows (Figure 2b):

(1) Select four DX and DLT cylindrical coal samples, respectively.

(2) Put coal samples into the centrifuge for 6 h.

(3) Conduct the NMR test.

(4) Put samples into a water saturator for 24 h.

(5) Conduct the NMR test again after drying the surface moisture on the samples.

(6) Put samples on the steam heating experimental platform and treat it according to Step (2) of the macroscopic crack experiment.

(7) Repeat Steps (2)−(5) on the shocked coal samples.

3. RESULTS AND DISCUSSION

3.1. Evolution Law of Macroscopic Fractures in Coal before and after Thermal Shock. After the cubic coal samples are photographed, the photos are processed by PCAS to extract the pore fractures. Photos taken before and after thermal shock of one face of the DLT coal sample and the extraction results are shown in Figure 3. For a clearer observation of the expansion of fractures, six faces of coal samples are expanded in line with surface photograph in Figure 2a to obtain Figure 4.

The analysis results in Figure 4 show that high-temperature steam shock on coal samples can effectively increase macroscopic fracture development. Compared with DX anthracite, high-temperature steam shock is more effective for DLT bituminous coal. This conclusion suggests that the degree of coalification should be an important consideration when deciding whether to use steam heat injection technology.

In Figure 4a, fractures of varying lengths can be observed on six faces of the DLT raw coal. Fractures on F1−F4 are mainly distributed horizontally, while the fractures distribution on F5 and F6 have no obvious pattern. Such a distribution is more obvious after thermal shock, and a large number of new fractures are generated, as shown in Figure 4b. Some of the new fractures expand along the original fractures, and the opening of the original fractures increases, which is more obvious on the main fractures. On F1 to F4, the main fractures are connected end to end, form a fracture surface. The main fractures zigzag indicates that the fracture surface is not flat, while the coal sample is not completely disconnected, which illustrates that the fracture extension is from the surface of the coal sample to the interior. This is because the sudden change of temperature during the thermal shock starts from the surface of the coal sample and conducts to the interior.

As indicated in Figure 4c, DX raw coal surface fractures are less and not fully developed. To be specific, there is no fracture on F3 and only one fracture on F2 and F5. After high-temperature shock, the fractures increase. As shown in Figure

https://doi.org/10.1021/acsomega.2c05849
ACS Omega 2022, 7, 44298−44309

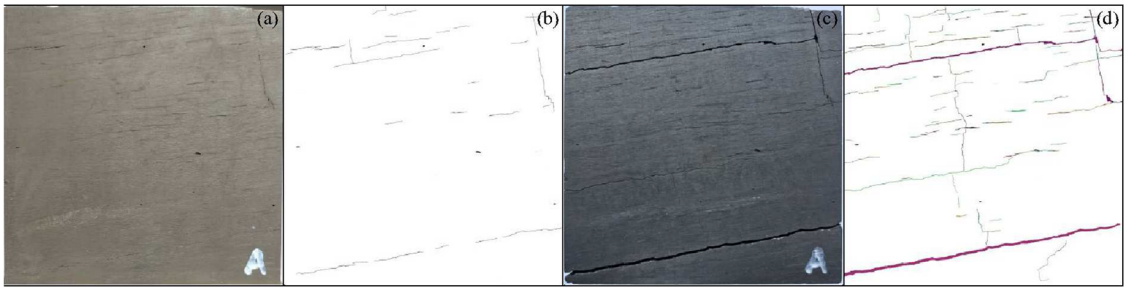

Figure 3. Fractures extraction effect of DLT coal sample. (a,b) are raw coal; (c,d) are thermal-shock coal.

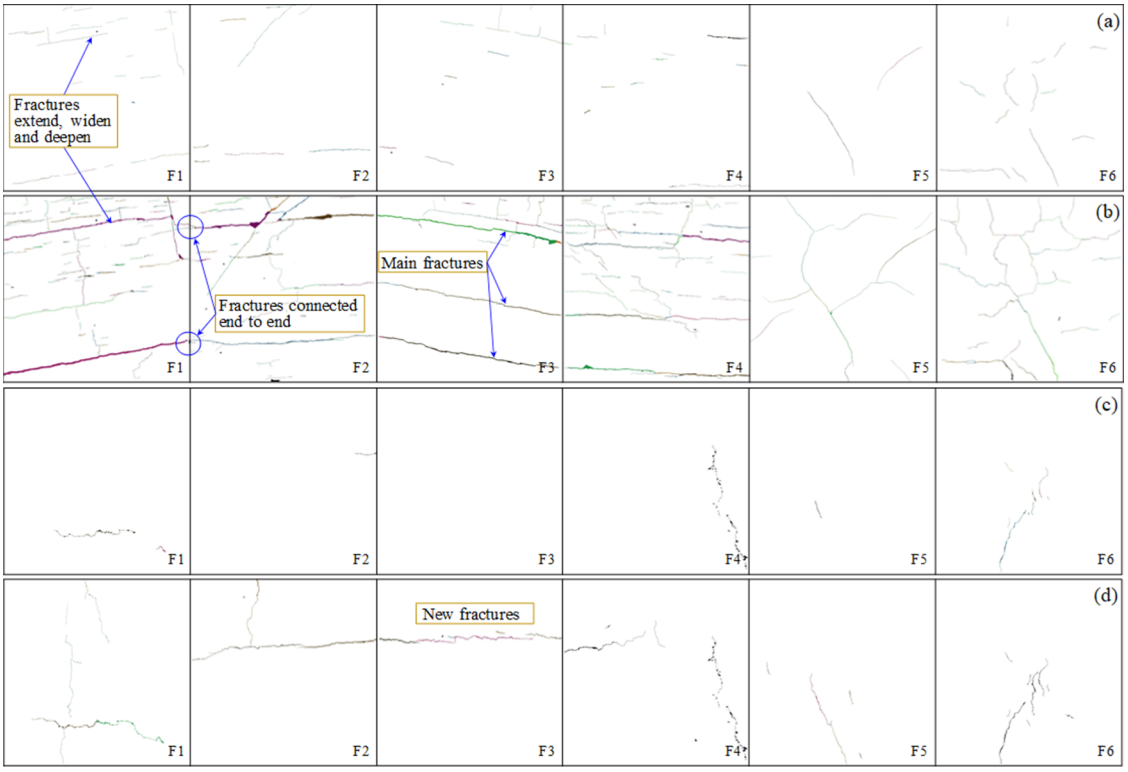

Figure 4. Comparison of surface fractures on coal samples before and after thermal shock. (a) DLT raw coal (DLT RC); (b) DLT high-temperature thermal shock coal (DLT HC); (c) DX raw coal (DX RC); (d) DX high-temperature thermal shock (DX HC).

4d, a fracture on F2 is connected with the fracture on F3, forming an almost straight line. Overall, the DX coal sample experiences a slighter fracture increase than the DLT coal sample, and surface fractures are distributed more unevenly for both DX raw coal and DX thermally shocked coal.

In order to further prove that thermal shock is more effective on DLT coal samples than DX coal samples, quantitative statistics are performed in six dimensions of fractures, that is, number, max width, max length, total length, area and surface porosity, as shown in Figure 5.

3.1.1. Fracture Area and Surface Porosity. The results of Figure 5a shows that the surface fracture area (unit: mm^2, converted by pixels) of coal samples increased significantly after thermal shock. The fracture area shares the same trend as the surface porosity, as shown in Figure 5a,c. Surface porosity, which is the ratio of fracture area to surface area of the coal sample, can characterize the permeability of the surface from a macroscopic perspective. As shown in Figure 5b, the surface porosities of DX and DLT coal samples have increased significantly after thermal shock, but the increases of different surfaces are quite different. The surface porosity of the whole coal sample is obtained by dividing the sum of fracture areas of the six faces of a coal sample by the sum of the total area of the six faces (Figure 5c). As indicated in Figure 5c, the surface porosities of DX RC and DX HC are 0.08 and 0.27%, respectively, an increase of 2.3 times, and those of DLT RC and DLT HC are 0.17 and 1.52%, respectively, an increase of 7.8 times.

3.1.2. Max Equivalent Fracture Width and Max Fracture Width. It can be seen from Figure 5d,e that the max equivalent fracture widths and the max fracture widths of both coal samples increase after thermal shock, DLT increasing more obviously. The equivalent fracture width, which equals the ratio of the area of a fracture to its length, can characterize changes of the surface fracture opening of coal samples. The max width in Figure 5e refers to the widest fracture on a certain face. The height of the histogram is the average value of six faces of the coal sample.

3.1.3. Probability Entropy (E). Figure 5f shows that the probability entropies of DLT and DX coal samples both increase after thermal shock, indicating a more chaotic direction of fracture expansion. Eq 1 is the mathematical expression of the probability entropy, which characterizes the direction of the fracture distribution:[32]

https://doi.org/10.1021/acsomega.2c05849
ACS Omega 2022, 7, 44298−44309

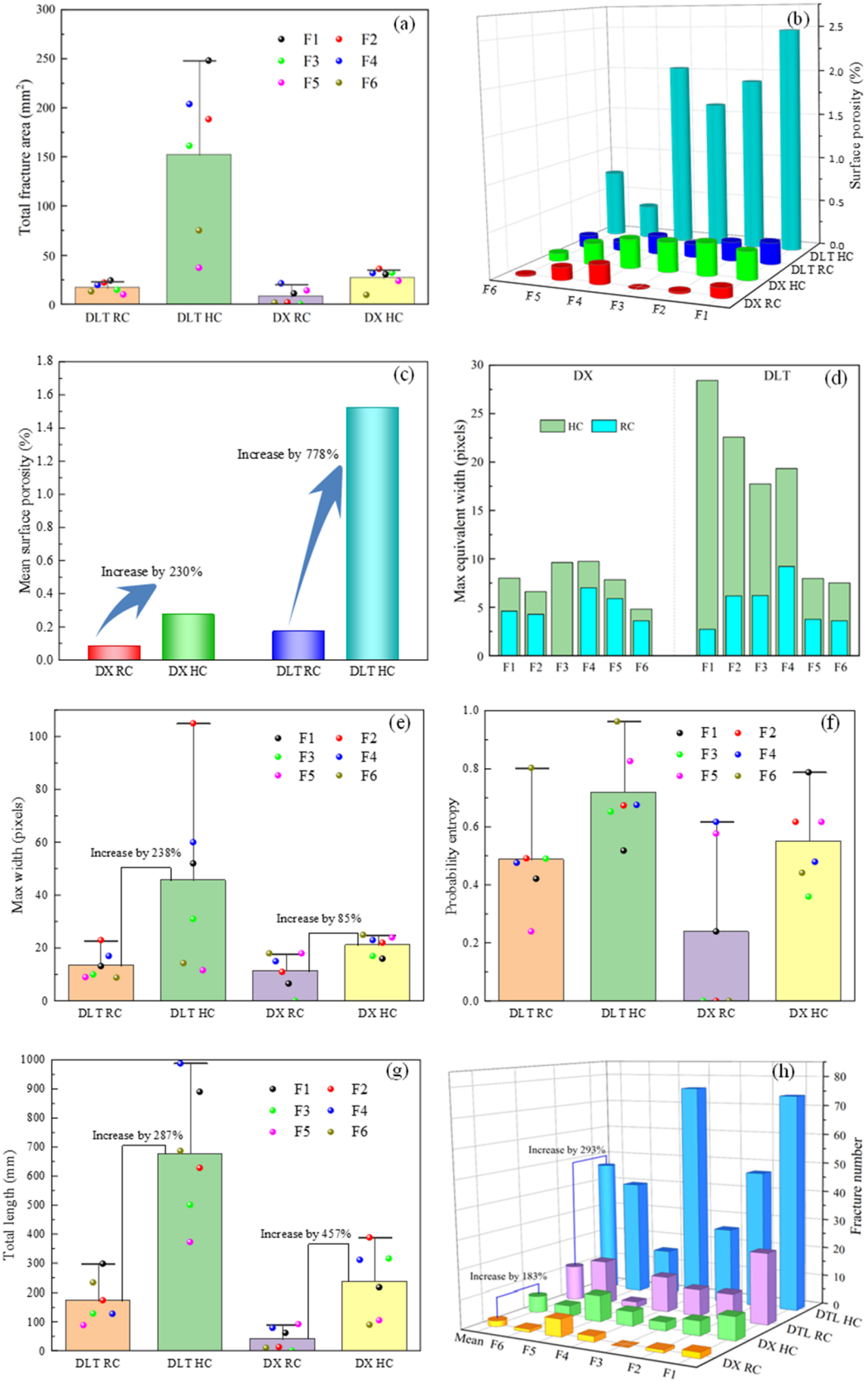

Figure 5. Statistics of surface fractures of coal samples. (a) Total fracture area; (b) Surface porosity; (c) Mean surface porosity; (d) Max equivalent width, which equals to the area of the fracture divided by its width; (e) Max width, which refers to the widest fracture on a surface; (f) Probability entropy of fractures; (g) Total length on a surface; (h) Fracture number.

https://doi.org/10.1021/acsomega.2c05849
ACS Omega 2022, 7, 44298−44309

$$E = -\sum_{i=1}^{18} P_i \log_{18}(P_i) \quad (1)$$

P_i is the ratio of pores and fractures to total pores and fractures in the ith direction interval.[32] The included angle between the straight line in a plane and the horizontal line of the plane ranges from 0° to 180°, and 180° is divided equally into 18 parts, where $i = 1$ indicates 0−10°, $i = 2$ indicates 10−20°, ..., $i = 18$ indicates 170−180°. The value of probability entropy lies in the range of 0−1. When $E = 1$, the fractures extension lines are in all directions, and when $E = 0$, all the fractures are in the same direction.

3.1.4. Total Fracture Lengths. Figure 5g shows changes of the total fracture lengths. The total fracture lengths of each face of DLT and DX coal samples increase by an average of 502.8 and 195.5 mm, respectively, after thermal shock.

3.1.5. Total Fracture Number. Figure 5h shows that the numbers of fractures in both coal samples increase. Specifically, the average number of fractures in one face of the DX coal sample increases from 2 to 5.67 by 183%, and that in one face of the DLT coal sample increases from 11.8 to 46.5 by 293%.

Figure 6 shows a partial enlarged view of the coal sample surface. A comparison between Figure 6a,b reveals that after

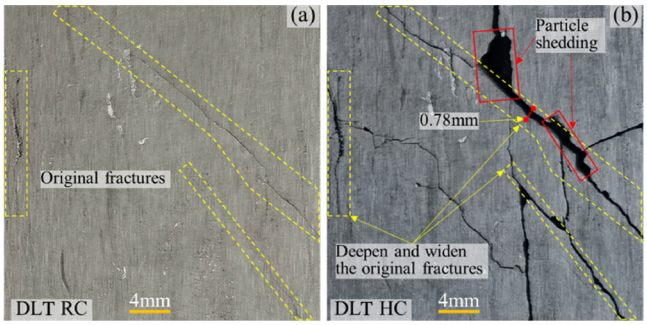

Figure 6. Comparison of partial fracture expansion (a) DLT RC; (b) DLT HC.

thermal shock, origin macroscopic fractures of the coal deepen and widen, and new fractures tend to expand along the direction of the original ones. Coal particles are shed from the surface of the coal sample, resulting in pits. The coal on both sides of the fracture experiences relative displacement to varying degrees, and the resulting gap is not closed after thermal shock. One of the possible reasons is that the shed coal particles are embedded in the gap to form a support. Such a self-supporting mode is of great significance to the formation of gas drainage network channel.

3.2. SEM Analysis of Coal Micro Pore−Fracture Structure Changes. SEM helps us directly observe the morphology of pore fractures from a microscopic perspective and compare the changes of pores and cracks before and after thermal shock.

Figure 7 is the SEM images of DLT and DX before and after thermal shock. The analysis of the four images shows that the pores of DLT raw coal are richer than those of DX raw coal. After thermal shock, DLT bituminous coal produces more fractures than DX anthracite, which is more suitable for high-temperature steam injection technology. Compared with Figure 7b,d, it can be found that after thermal shock, DLT develops more pores and fractures, which increase the specific surface area of coal and are conducive to gas desorption in coal. Fractures are interconnected, providing a channel for gas migration. The direct cause of fractures propagation is that the thermal stress produced during thermal shock exceeds the tensile strength of coal. After thermal shock under the same conditions, DLT HC developed crisscross fractures (Figure 7b), while DX HC had only one fracture (Figure 7d), mainly because the tensile strength of DX is greater than that of DLT (which will be further discussed in Section 3.4). In addition, it is also related to the development degree of primary pores and fractures (Figure 7a,c) and the content of four components in the proximate analysis of coal (Table 1). The higher the moisture and volatile content of coal, the weaker the intermolecular force of coal, and the easier the coal body to fractures.[33] The moisture and volatile matter in coal are easy to volatilize under high temperature, which affects the pore−fracture structure of coal.

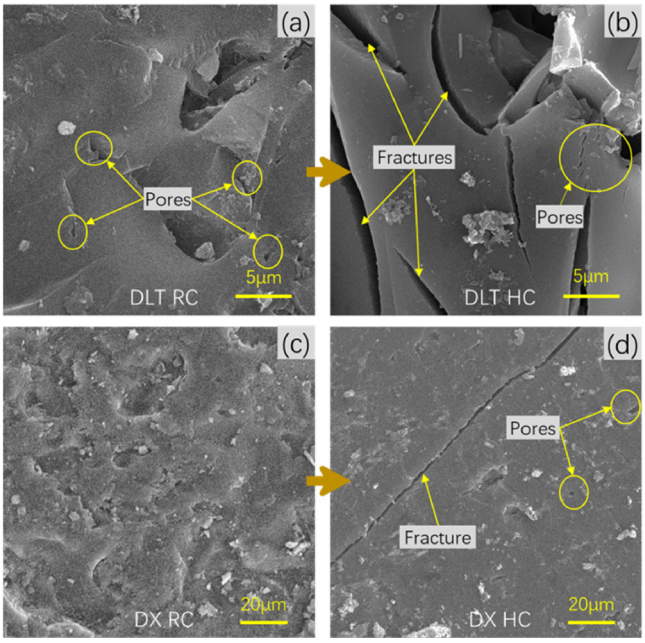

Figure 7. SEM images before and after thermal shock. (a) DLT RC; (b) DLT HC; (c) DX RC; (d) DX HC.

It can be concluded from Figure 8 that minerals have a great influence on the development of pores and fractures in coal

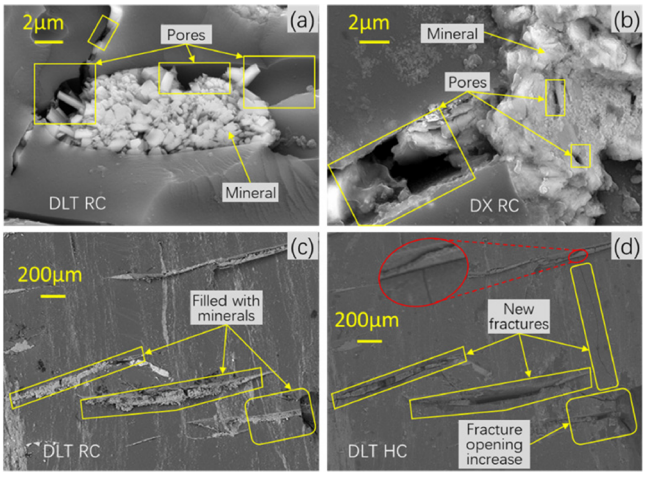

Figure 8. Changes of pores and fractures around minerals. (a) DLT RC; (b) DX RC; (c) DLT RC; (d) DLT HC.

https://doi.org/10.1021/acsomega.2c05849
ACS Omega 2022, 7, 44298−44309

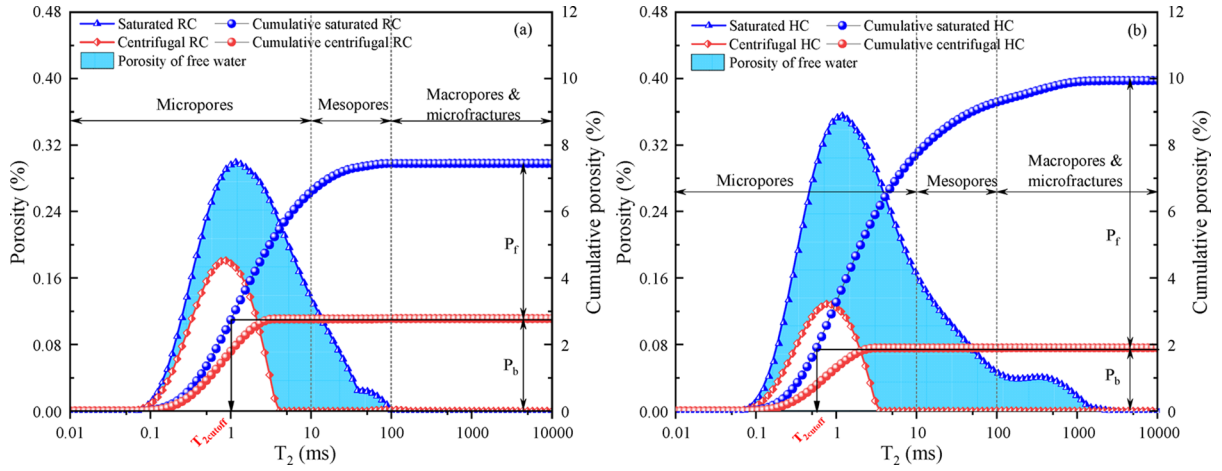

Figure 9. Porosity changes of bound water and free water of DLT-1 samples before and after thermal shock: (a) porosity of raw coal; (b) porosity of shocked coal; P_b: porosity of bound water; P_f: porosity of free water.

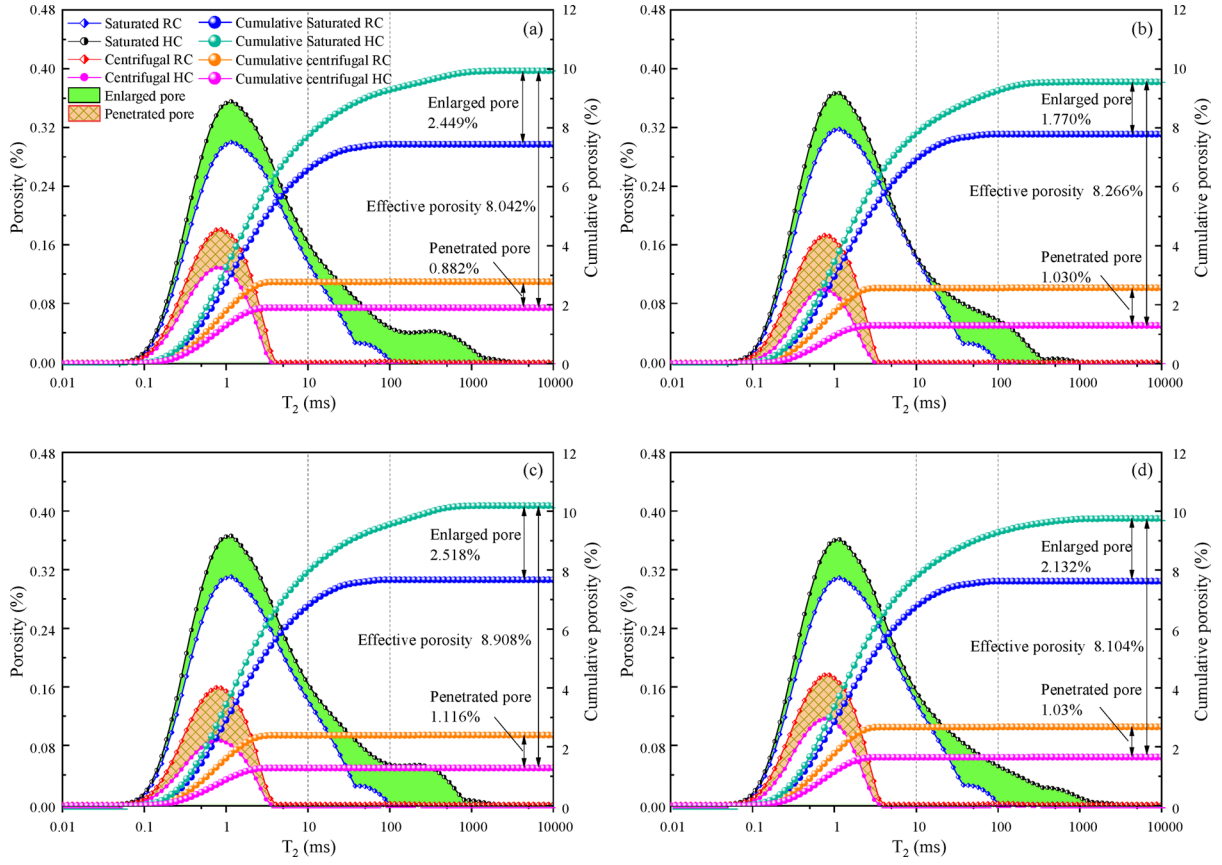

Figure 10. Porosity changes of four DLT bituminous coal samples before and after high-temperature steam shock: (a) DLT-1; (b) DLT-2; (c) DLT-3; (d) DLT-4.

during thermal shock, and fractures are easier to expand along the interface of minerals. The type and content of minerals is one of the key factors affecting the effect of thermal shock. It can be seen from Figure 8a,b that the minerals are embedded in the primary pores and fissures of the coal. The interface between the two is not completely consistent, but there are pores of various shapes, which become a part of the gas storage space. In Figure 8c, the minerals are banded in the coal. After thermal shock, fractures are obviously developed at the interface between minerals and coal matrix (Figure 8d), while the original fracture opening is increased. This is mainly because the thermal expansion coefficients of coal matrix and minerals are different. During the heating process, the expansion and deformation of coal matrix and minerals are inconsistent, resulting in thermal stress. In addition, on the interface between coal matrix and minerals, it is often not as solid as a single material. Therefore, cracks are easier to develop along the interface. The greater the difference between the thermal expansion coefficients of coal and minerals, the easier the cracks appear. These fissures provide channels for gas migration and enhance the permeability of coal.

3.3. Evolution Law of Micropores of Coal after High-Temperature Steam. In the T_2 NMR spectra, it is generally

https://doi.org/10.1021/acsomega.2c05849
ACS Omega 2022, 7, 44298−44309

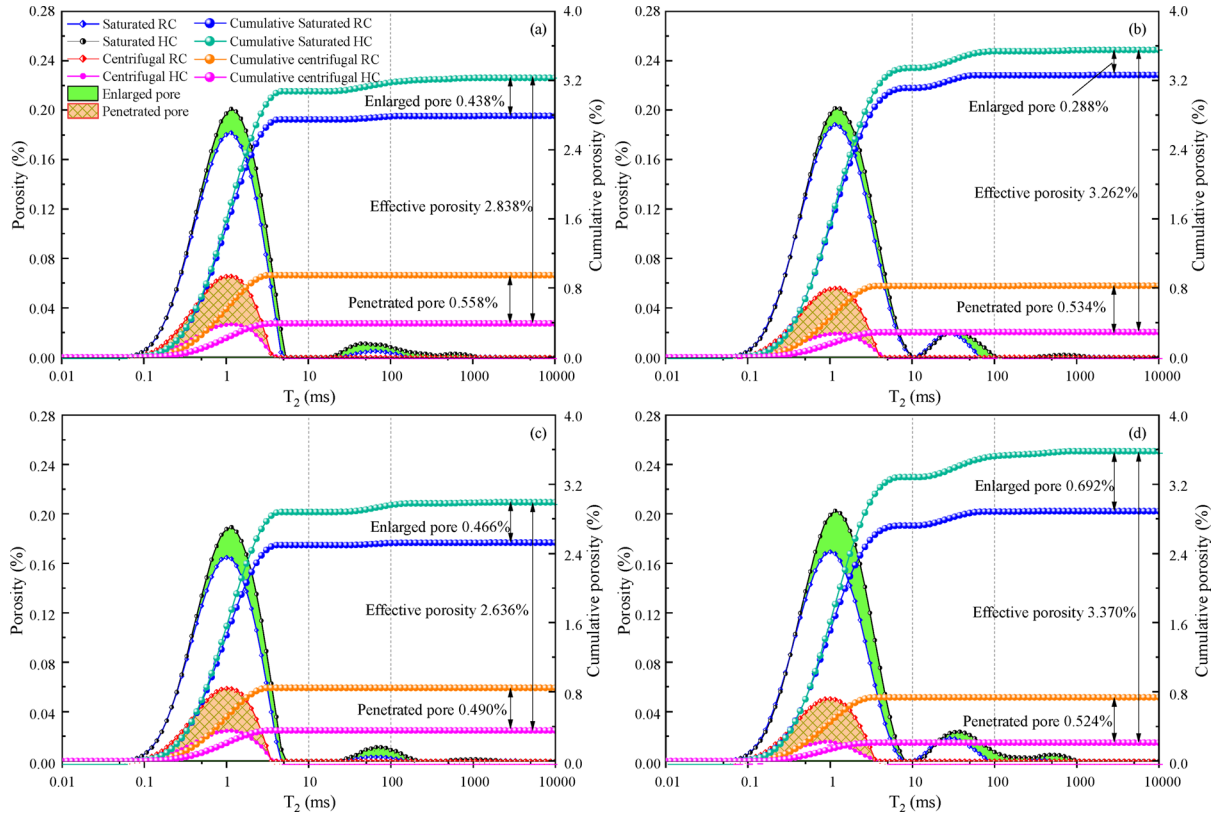

Figure 11. Porosity changes of four DX anthracite coal samples before and after high-temperature steam shock: (a) DX-1; (b) DX-2; (c) DX-3; (d) DX-4.

considered that the section where T_2 is less than 10 ms belongs to the micropore section, where T_2 is 10−100 ms belongs to the meso-pore section and where T_2 is greater than 100 ms belongs to the macro-pore and micro-fracture section.

Figure 9 shows the test results of DLT-1 coal sample before and after high-temperature steam shock. Comparing and analyzing the two graphs, it can be concluded that the pores connectivity in the coal is enhanced after the high-temperature steam shock, which is beneficial to the desorption and transport of gas. The saturated pores contain free water and bound water. Free water, which is stored in interconnected pores in the coal sample, can be removed through centrifugation or drying. The interconnected pores provide channels for gas transport. While bound water, which is generally unmovable water stored in closed pores or macromolecules, cannot be removed. The closed pore space cannot constitute a channel for gas transport, which is different from the view of ZHANG X, who regarded all saturated water pore spaces as effective pore spaces (connected pore spaces).[34] As indicated in Figure 9a, the pores are mainly micropores and mesopores, the former accounting for a large proportion, and neither macropores nor micro-fractures develop. In Figure 9b, micropores, mesopores and macropores all develop, and more macropores appear after thermal shock. Comparing Figures 9a and 7b, the free water area of the thermally shocked coal is larger than that of the raw coal, and the unimodal distribution in the T_2 spectrum of the raw coal changes into a bimodal distribution after thermal shock.

The abscissa of the intersection point between the extension line of the horizontal section of the cumulative centrifugal curve and the cumulative saturated curve represents the cut-off value of T_2 whose value can reflect the distribution relationship between the number of interconnected pores and closed pores in the pore structure. The smaller the value, the more the interconnected pores. By comparing Figures 9a and 7b, it can be seen that after thermal shock, the $T_{2cutoff}$ value moves leftward on the T_2 spectrum (from 1 to 0.57 ms on the abscissa), indicating that the ratio of free water volume to bound water volume index increases gradually, and the pores connectivity inside the coal is enhanced.

To facilitate the comparison, the T_2 spectra of coal samples before and after thermal shock are drawn on the same figure for analysis (Figures 10 and 11). In the figure, the area formed by the saturated RC curve and the saturated HC curve is the newly increased enlarged-pore porosity. This area is caused by the increase of the volume of original pores or the generation of new pores during thermal shock, representing the enlarged pores. The area formed by the centrifugal RC curve and the centrifugal HC curve is the penetrated-pore porosity, representing the newly connected pores. That is, under thermal shock, the closed pores are opened, and the original bound water is transformed into free water. Therefore, it is concluded that the effective porosity after thermal shock is composed of three parts, namely effective porosity of the raw coal, enlarged-pore porosity and penetrated-pore porosity.

Through statistical calculation, the variances of the enlarged pore and penetrated pore of the four DLT coal samples are 8.79×10^{-6} and 7.08×10^{-7}, respectively, and the variance of the enlarged pore and penetrated pore of the four DX coal samples are 2.09×10^{-6} and 5.97×10^{-7}. The variance values are very small, indicating that the experimental results are reliable.

As displayed in Figure 10, after thermal shock, the peak value of the centrifugal curve is far lower than that of the raw coal, while the saturated curve is notably higher than that of the raw coal, especially in the micropore, mesopore and macro-pore

https://doi.org/10.1021/acsomega.2c05849
ACS Omega 2022, 7, 44298−44309

sections. That is, after thermal shock, the enlarged-pore porosity and penetrated-pore porosity areas of the DLT coal sample increase remarkably.

Figure 11 shows the change trends of T_2 curves of DX RC and DX HC. The T_2 curve of saturated RC is mainly distributed in the micropore section and sparely distributed in the mesopore section. Only two peaks are present in the whole T_2 spectrum. After thermal shock, the area enclosed by T_2 curves of saturated RC grows slightly, which is distributed in the micropore, mesopore and macro-pore sections, and three peaks are present. The saturated HC curve enlarges compared with the saturated RC curve; the centrifugal HC curve is lower than the centrifugal RC curve; and the increase of penetrated-pore area is more significant.

Enlarged/penetrated refers to the ratio of enlarged-pore porosity to penetrated-pore porosity. When Enlarged/penetrated >1, the increased pores are dominated by enlarged pores; when Enlarged/penetrated <1, the increased pores are dominated by penetrated pores.

The effective porosity after thermal shock is illustrated in Figure 10, which is stacked by RC effective porosity, enlarged-pore porosity and penetrated-pore porosity. The axis percentage of the growth ratio in Figure 10 is the growth ratio of HC porosity to RC porosity, and the growth part is the sum of enlarged-pore porosity and penetrated-pore porosity. From Figure 12, the porosity, growth ratio and Enlarged/penetrated of

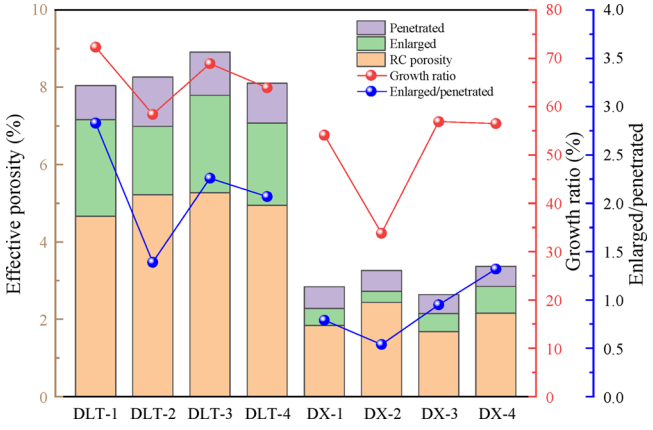

Figure 12. Proportions of enlarged pores and penetrated pores in effective porosity. Enlarged/penetrated: ratio of enlarged-pore porosity to penetrated-pore porosity.

the DLT coal sample are higher than those of the DX coal sample, be it RC or HC, which suggests that DLT bituminous coal is more sensitive to the thermal shock than the DX anthracite coal.

Average values of pore parameters of DLT and DX coal samples are given in Table 2.

From the average values of Table 2, it can be concluded that the effect of high-temperature steam impact on DLT bituminous coal is better than that of DX anthracite. The average porosity growth rate of the DLT coal sample (65.9%) is higher than that of the DX coal sample (50.3%). In addition, the average ratios of enlarged-pore porosity to penetrated-pore porosity for the DLT and DX coal samples are 2.14 and 0.9, indicating that the porosity change of DLT bituminous coal is dominated by enlarged pores after thermal shock, while DX anthracite coal is dominated by penetrated pores.

Based on the data in Figure 13, the influence of enlarged pores during thermal shock can be explored. For the DLT bituminous

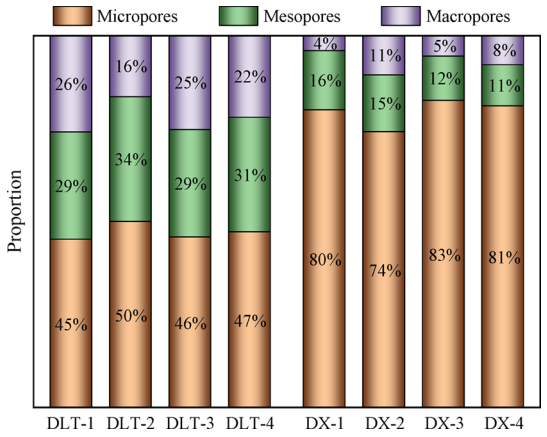

Figure 13. Proportions of macropores, mesopores and micropores in the enlarged pores.

coal and the DX anthracite coal, the enlarged pores influence micropores mostly and macropores least. Specifically, the average proportions of micropores, mesopores and macropores in the enlarged pores are 47.1, 30.5, 22.3% for the DLT bituminous coal and 79.6, 13.5 and 6.9% for the DX anthracite coal, respectively. A comparison between the average values of the two kinds of coal discloses that macropores and mesopores develop better in the DLT bituminous coal than in the DX anthracite coal.

The amount of penetration refers to the number of free water pores transformed from bound water pores under thermal shock, that is, the penetration rate is equal to the proportion of bound water in the RC minus that in the HC. The conversion rate is the ratio of the penetration amount of bound water pores to the total amount of bound water pores of RC. This index can be used to measure the efficiency of thermal shock to unclog closed pores. The amounts of penetration and conversion rates of coal samples are calculated (Figure 14). In terms of the amount of penetration, the average amounts of penetration of the DLT and DX coal samples are 1.076 and 0.527%, respectively, the former being larger than the latter. According to the area of penetrated pores in Figures 10 and 11, the DLT RC sample contains more bound water than the DX RC sample. However, in terms of the conversion rate in Figure 12, the conversion rate of the DLT coal sample is significantly lower than that of the DX coal sample. The average conversion rate of the four DLT coal samples is 41.6%, while that of four DX coal samples is 63.2%. The above results suggest that although the DLT coal sample corresponds to the transformation of more

Table 2. Average Values of DLT and DX Pore Parameters

type	RC porosity (%)	enlarged (%)	penetrated (%)	effective porosity (%)	growth ratio (%)	enlarged/penetrated
DLT average	5.03	2.228	1.076	8.32	65.9	2.14
DX average	2.03	0.472	0.526	3.02	50.3	0.90

https://doi.org/10.1021/acsomega.2c05849
ACS Omega 2022, 7, 44298−44309

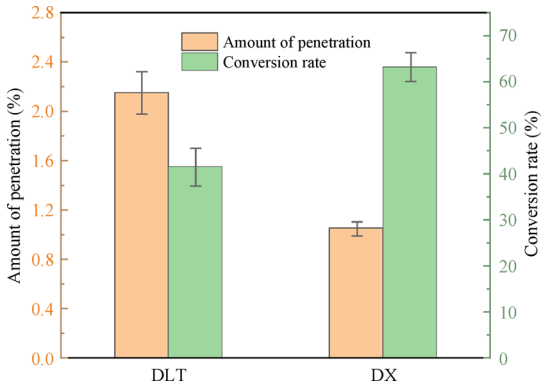

Figure 14. Amounts of penetration and conversion rates of penetrated pores.

bound water pores into free water pores, its conversion rate is lower than that of the DX coal sample.

Figure 15 shows changes of effective porosities of eight RC samples and eight HC samples. The analysis results show that,

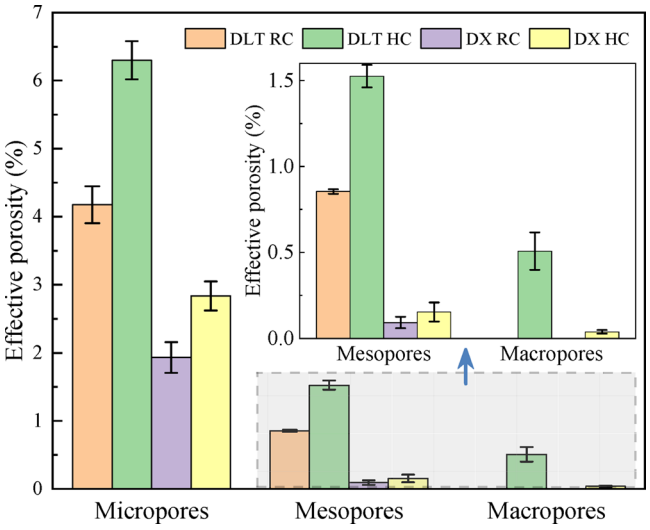

Figure 15. Effective porosity distribution.

after high-temperature steam shock, the total volumes of macropores, mesopores and micropores all increase, the absolute increment of micropores being the largest and that of macropores being the smallest. Based on the analysis of Figures 10 and 11, it can be concluded that during thermal shock, some micropores are transformed into mesopores and some mesopores are transformed into macropores; in addition, micropores and mesopores develop further.

3.4. Analysis of the Mechanism of Pore−Fracture Change under High-Temperature Steam Shock. Coal, whose compressive strength is weaker than tensile strength, is a kind of brittle material with original pore−fracture structure. Under the temperature shock, its original pore−fracture structure will change. Coal expands with heat and contracts with cold. In other words, it produces compressive stress when cooling and tensile stress when heating. Due to the heterogeneity of coal, different components correspond to different thermal expansion coefficients and different heat transfer efficiencies during the cooling and heating process, which leads to the heterogeneous deformation between minerals. As the interactions between minerals and between minerals and coal matrix are restrained, the thermal stress in coal is formed. When the thermal stress exceeds the compressive or tensile strength of the coal, its original pore−fracture structure will preferentially expand and deform, the fracture will widen, and new fractures will emerge along the fracture tip and mineral particle boundary, damaging the internal structure of the coal. This is called the thermal breakdown phenomenon (Figure 16).

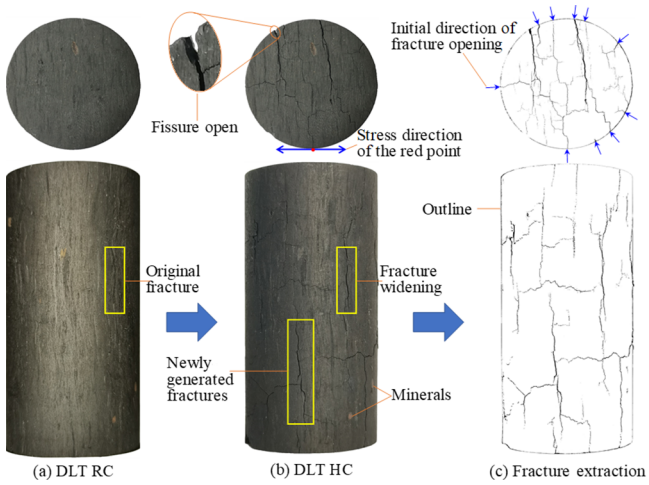

Figure 16. Thermal breakdown of coal shocked by high-temperature steam.

In the light of the thermal stress theory, the breaking of the coal sample under high-temperature steam shock belongs to the category of unsteady thermal stress. The thermal stress of the test coal sample under the temperature shock can be calculated by eq 2:[35,36]

$$\left.\begin{aligned}\sigma_r &= \frac{\alpha E}{1-\mu}\frac{2h^2\Delta T}{b^2}\sum_{n=1}^{\infty}\frac{e^{-\kappa g_n^2 t}}{(g_n^2+b_n^2)g_n^2 J_1(g_n^2 b)} \times\left[\frac{b}{r}J_1(g_n r)-J_1(g_n b)\right]\\ \sigma_\theta &= \frac{\alpha E}{1-\mu}\frac{2h^2\Delta T}{b^2}\sum_{n=1}^{\infty}\frac{e^{-\kappa g_n^2 t}}{(g_n^2+b_n^2)g_n^2 J_1(g_n^2 b)} \times\left[g_n b J_0(g_n r)-\frac{b}{r}J_1(g_n r)-J_1(g_n b)\right]\end{aligned}\right\} \quad (2)$$

where σ_r is the thermal stress of the coal sample in the radial direction; σ_θ is the thermal stress of the coal sample in the tangential direction perpendicular to the direction of σ_r; E is the modulus of elasticity; κ is the thermal conductivity coefficient; b is the radius of the cylindrical coal sample; μ is Poisson's ratio; α is the linear expansion coefficient; h is the heat release coefficient; r is the distance from any point in the cross section of the coal sample to the center of the cross section ($0 \le r \le b$); ΔT is the temperature difference, that is, temperature gradient; $J_0(g_n r)$ and $J_1(g_n r)$ are the first zero-order Bessel function and the first one-order Bessel function, respectively; g_n is the positive root of eq 3:

$$g_n J_1(g_n r) - hJ_0(g_n b) = 0 \quad (3)$$

The solution of internal thermal stress of the coal sample can be calculated by combining eqs 2 and 3:

https://doi.org/10.1021/acsomega.2c05849
ACS Omega 2022, 7, 44298−44309

$$\left.\begin{aligned}(\sigma_r)_{max} &= 0.2356\frac{\alpha E\Delta T}{1-\mu}\left(t = 0.0764\frac{b^2}{\alpha}\right)\\ (\sigma_\theta)_{max} &= -\frac{\alpha E\Delta T}{1-\mu}\ (t = 0)\end{aligned}\right\} \quad (4)$$

where the negative sign (−) denotes the tensile stress.

According to eq 4, the max thermal stress generated in the coal sample is σ_θ, which is consistent with the wide opening of the initial fracture in the experiment. The max width of the fracture appears at the edge of the cylindrical coal sample (Figure 16b). The maximum thermal stress is located on the surface of the coal sample, and the initial direction of the fracture opening on the coal sample surface points to the central axis of the coal sample (Figure 16c). The α, E and μ of the DX anthracite coal and the DLT bituminous coal are measured by dilatometer and triaxial compression test (Table 3).

Table 3. Thermodynamic Parameters of Coal Samples

parameter	α (°C^{-1})	E(GPa)	μ	tensile strength (MPa)
DX	1.5×10^{-5}	1.90	0.21	0.82
DLT	2.4×10^{-5}	1.02	0.31	0.46

During heating, the temperature shock on the coal surface equals the difference between the steam exit temperature and the room temperature, that is ΔT = 177 °C. When the autoclave is depressurized and cools, the internal high pressure is connected with the external atmospheric pressure, and the superheated water on the coal surface evaporates rapidly. After the evaporation, the temperature of the coal is 100 °C, and the shock temperature ΔT is 103 °C. Substituting the above parameters into eq 4, the thermal stresses under different temperature shocks are obtained. When ΔT = 177 °C, the thermal stresses of the DX anthracite coal and the DLT bituminous coal are 6.91 and6.28 MPa, respectively, being the largest. When ΔT = 103 °C, their thermal stresses are 4.02 and 3.65 MPa, respectively. Both are greater than the tensile strength of the two coal samples, indicating that the coal sample has formed new fractures and achieved pressure relief.

The differences in the numbers and shapes of fractures the DX anthracite coal and the DLT bituminous coal are mainly attributed to the differences in their components, original pore−fracture structures and physical and mechanical parameters. As listed in Tables 1 and 3, the elastic modulus and fixed carbon content of the DX are higher than those of the DLT bituminous coal, while the volatile matter content of the DX is much lower than that of the DLT. A higher carbon content of RC is indicative of a greater elastic modulus, a structure closer to that of graphite and stronger compressive and tensile strengths, whereas the volatile matter content is negatively correlated with the tensile strength.[37] Therefore, in general, low-rank coal is more suitable for high-temperature steam injection technology.

4. CONCLUSIONS

This study investigated the change laws of the pore−fracture structure of coal under high-temperature steam shock from the macro and micro perspectives. The principal conclusions are as follows.

(1) High-temperature steam shock results in the occurrence, widening, and extension of coal fractures, which can effectively improve the porosity of coal, and is significantly better for bituminous coal than anthracite.

(2) The increased pores induced by high-temperature steam shock are of enlarged and penetrated types. Enlarged pores increase the volume or number of pores, while penetrated pores are opened pores that used to be closed in which pores and fractures become connected.

(3) After high-temperature steam impact on coal, the absolute numbers of macropores, mesopores, and micropores all increase. Micropores experience the largest increment followed by mesopores, and macropores correspond to the smallest increment.

(4) The thermal stress exceeds the tensile strength of the coal sample, resulting in the generation and expansion of pores and fractures. Heterogeneous distribution of mineral components, different thermal expansion and contraction coefficients of the coal, and the temperature gradient during the process induce heterogeneous and uncoordinated deformation between mineral grains, which stand to be the fundamental mechanism behind thermal stress-induced coal breaking.

The research outcome of this study could provide theoretical support for enhanced gas extraction technology by high-temperature steam injection into coal seams. Future studies will be focusing on the study of gas, steam and water transport, and heat flow solid coupling in the coal after steam injection into the coal seam.

AUTHOR INFORMATION

Corresponding Author

Baiquan Lin − *Key Laboratory of Coal Methane and Fire Control, Ministry of Education and School of Safety Engineering, China University of Mining and Technology, Xuzhou, Jiangsu 221116, China;* orcid.org/0000-0002-7553-5080; Email: lbq21405@126.com

Authors

Youping Xu − *Key Laboratory of Coal Methane and Fire Control, Ministry of Education and School of Safety Engineering, China University of Mining and Technology, Xuzhou, Jiangsu 221116, China;* orcid.org/0000-0002-7325-0241

Yuxue Li − *School of Humanities and Arts, China University of Mining and Technology, Xuzhou, Jiangsu 221116, China*

Complete contact information is available at: https://pubs.acs.org/10.1021/acsomega.2c05849

Author Contributions

Y.X. was involved in conceptualization, methodology preparation, investigation, and writing the original draft, reviewing, and editing. B.L. was involved in resource procurement, writing, reviewing, and editing, and funding acquisition. Y.L. was involved in investigation.

Notes

The authors declare no competing financial interest.

ACKNOWLEDGMENTS

The authors gratefully acknowledge the financial support from the National Natural Science Foundation of China (51474211), the Graduate Innovation Program of China University of Mining and Technology (2022WLKXJ102), and the Post-

https://doi.org/10.1021/acsomega.2c05849
ACS Omega 2022, 7, 44298−44309

graduate Research & Practice Innovation Program of Jiangsu Province (2022 KYCX22_2661).

REFERENCES

(1) Feng, Z. C.; Zhou, D.; Zhao, Y. S.; Cai, T. T. Study on microstructural changes of coal after methane adsorption. *J. Nat. Gas Sci. Eng.* **2016**, *30*, 28−37.
(2) Sun, W. J.; Feng, Y. Y.; Jiang, C. F.; Chu, W. Fractal characterization and methane adsorption features of coal particles taken from shallow and deep coalmine layers. *Fuel* **2015**, *155*, 7−13.
(3) Mitra, A.; Harpalani, S.; Liu, S. M. Laboratory measurement and modeling of coal permeability with continued methane production: Part 1-Laboratory results. *Fuel* **2012**, *94*, 110−116.
(4) Wang, D. K.; Wei, J. P.; Fu, Q. C.; Liu, Y.; Xia, Y. L. Seepage law and permeability calculation of coal gas based on Klinkenberg effect. *J. Cent. South Univ.* **2015**, *22*, 1973−1978.
(5) Lu, Y.; Li, H.; Lu, J. X.; Shi, S. L.; Wang, G. G. X.; Ye, Q.; Li, R. Q.; Zhu, X. N. Clean up water blocking damage in coalbed methane reservoirs by microwave heating: Laboratory studies. *Process Saf. Environ. Prot.* **2020**, *138*, 292−299.
(6) Bahrami, H.; Rezaee, R.; Clennell, B. Water blocking damage in hydraulically fractured tight sand gas reservoirs: An example from Perth Basin, Western Australia. *J. Pet. Sci. Eng.* **2012**, *88*−*89*, 100−106.
(7) Huang, W. A.; Lei, M.; Qiu, Z. S.; Leong, Y. K.; Zhong, H. Y.; Zhang, S. F. Damage mechanism and protection measures of a coalbed methane reservoir in the Zhengzhuang block. *J. Nat. Gas Sci. Eng.* **2015**, *26*, 683−694.
(8) Kang, Y. L.; Xu, C. Y.; You, L. J.; Yu, H. F.; Zhang, B. J. Comprehensive evaluation of formation damage induced by working fluid loss in fractured tight gas reservoir. *J. Nat. Gas Sci. Eng.* **2014**, *18*, 353−359.
(9) Liu, Q.; Guo, Y.; An, F.; Lin, L.; Lai, Y. Water blocking effect caused by the use of hydraulic methods for permeability enhancement in coal seams and methods for its removal. *Int. J. Min. Sci. Technol.* **2016**, *26*, 615−621.
(10) Zhao, D.; Zhang, C.; Chen, H.; Feng, Z. C. Experimental study on gas desorption characteristics for different coal particle sizes and adsorption pressures under the action of pressured water and superheated steam. *J. Pet. Sci. Eng.* **2019**, *179*, 948−957.
(11) Cai, Y. D.; Liu, D. M.; Yao, Y. B.; Li, Z. T.; Pan, Z. J. Partial coal pyrolysis and its implication to enhance coalbed methane recovery, Part I: An experimental investigation. *Fuel* **2014**, *132*, 12−19.
(12) Li, H.; Lin, B. Q.; Yang, W.; Hong, Y. D.; Wang, Z. A fully coupled electromagnetic-thermal-mechanical model for coalbed methane extraction with microwave heating. *J. Nat. Gas Sci. Eng.* **2017**, *46*, 830−844.
(13) Hong, Y. D.; Lin, B. Q.; Zhu, C. J.; Li, H. Effect of microwave irradiation on petrophysical characterization of coals. *Appl. Therm. Eng.* **2016**, *102*, 1109−1125.
(14) Zhao, S.; Chen, X. J.; Li, X. J.; Qi, L. L.; Zhang, G. X. Experimental analysis of the effect of temperature on coal pore structure transformation. *Fuel* **2021**, *305*, No. 121613.
(15) Mu, Y. L.; Fan, Y. P.; Wang, J. R.; Fan, N. Numerical study on injection of flue gas as a heat carrier into coal reservoir to enhance CBM recovery. *J. Nat. Gas Sci. Eng.* **2019**, *72*, No. 103017.
(16) Liu, X. Q.; Li, M. J.; Zhang, C. H.; Fang, R. H.; Zhong, N. N.; Xue, Y.; Zhou, Y.; Jiang, W. D.; Chen, X. Y. Mechanistic insight into the optimal recovery efficiency of CBM in sub-bituminous coal through molecular simulation. *Fuel* **2020**, *266*, No. 117137.
(17) Xu, Y. P.; Lin, B. Q.; Liu, T. Evolutions of Pore and Crack Structure of Coal under Hot Steam Heating. *Energy Fuels* **2022**, *36*, 1417.
(18) Lin, B. Q.; Li, H.; Chen, Z. W.; Zheng, C. S.; Hong, Y. D.; Wang, Z. Sensitivity analysis on the microwave heating of coal: A coupled electromagnetic and heat transfer model. *Appl. Therm. Eng.* **2017**, *126*, 949−962.
(19) Hong, Y. D.; Lin, B. Q.; Li, H.; Dai, H. M.; Zhu, C. J.; Yao, H. Three-dimensional simulation of microwave heating coal sample with varying parameters. *Appl. Therm. Eng.* **2016**, *93*, 1145−1154.
(20) Li, H.; Lin, B. Q.; Chen, Z. W.; Hong, Y. D.; Zheng, C. S. Evolution of Coal Petrophysical Properties under Microwave Irradiation Stimulation for Different Water Saturation Conditions. *Energy Fuels* **2017**, *31*, 8852−8864.
(21) Liu, J. Z.; Zhu, J. F.; Cheng, J.; Zhou, J. H.; Cen, K. F. Pore Structure and Fractal Analysis of Ximeng Lignite under Microwave Irradiation. *Fuel* **2015**, *146*, 41−50.
(22) Lu, J. X.; Li, H.; Shi, S. L.; Huang, B. X.; Lu, Y.; Li, M.; Ye, Q. Microwave-Induced Microstructure Evolution of Coal and Its Effects on the Methane Adsorption Characteristic. *Energy Fuels* **2021**, *35*, 4081−4090.
(23) Fu, X. X.; Lun, Z. M.; Zhao, C. P.; Zhou, X.; Wang, H. T.; Zhou, X. T.; Xu, Y.; Zhang, H.; Zhang, D. F. Influences of controlled microwave field irradiation on physicochemical property and methane adsorption and desorption capability of coals: Implications for coalbed methane (CBM) production. *Fuel* **2021**, *301*, No. 121022.
(24) Salmachi, A.; Haghighi, M. Feasibility Study of Thermally Enhanced Gas Recovery of Coal Seam Gas Reservoirs Using Geothermal Resources. *Energy Fuels* **2012**, *26*, 5048−5059.
(25) Wang, D. K.; Yao, B. H.; Gao, Y. N.; Li, W. R.; Lv, R. H. Effect of Cyclic Temperature Impact on Coal Seam Permeability. *Therm. Sci.* **2017**, *21*, S351−S357.
(26) Shahtalebi, A.; Khan, C.; Dmyterko, A.; Shukla, P.; Rudolph, V. Investigation of thermal stimulation of coal seam gas fields for accelerated gas recovery. *Fuel* **2016**, *180*, 301−313.
(27) Cai, Y. D.; Liu, D. M.; Liu, Z. H.; Zhou, Y. F.; Che, Y. Evolution of pore structure, submaceral composition and produced gases of two Chinese coals during thermal treatment. *Fuel Process. Technol.* **2017**, *156*, 298−309.
(28) Teng, T.; Wang, J. G.; Gao, F.; Ju, Y. Complex thermal coal-gas interactions in heat injection enhanced CBM recovery. *J. Nat. Gas Sci. Eng.* **2016**, *34*, 1174−1190.
(29) Daigle, H.; Johnson, A.; Thomas, B. Determining fractal dimension from nuclear magnetic resonance data in rocks with internal magnetic field gradients. *Geophysics* **2014**, *79*, D425−D431.
(30) Li, S.; Tang, D. Z.; Pan, Z. J.; Xu, H.; Huang, W. Q. Characterization of the stress sensitivity of pores for different rank coals by nuclear magnetic resonance. *Fuel* **2013**, *111*, 746−754.
(31) Yao, Y. B.; Liu, D. M.; Che, Y.; Tang, D. Z.; Tang, S. H.; Huang, W. H. Petrophysical characterization of coals by low-field nuclear magnetic resonance (NMR). *Fuel* **2010**, *89*, 1371−1380.
(32) Sun, Y.; Zhai, C.; Xu, J. Z.; Cong, Y. Z.; Zheng, Y. F. Experimental study on pore structure evolution of coal in macroscopic, mesoscopic, and microscopic scales during liquid nitrogen cyclic cold-shock fracturing. *Fuel* **2021**, *291*, No. 120150.
(33) Lin, Y. B.; Qin, Y.; Qiao, J. W.; Li, G.; Zhang, H. Effect of coalification and maceration on pore differential development characteristics of high-volatile bituminous coal. *Fuel* **2022**, *318*, No. 123634.
(34) Zhang, X. L.; Lin, B. Q.; Li, Y. J.; Zhu, C. J.; Li, Q. Z. Analysis of fractal dimension of coal subjected to electrical breakdown based on nuclear magnetic resonance. *J. Nat. Gas Sci. Eng.* **2020**, *79*, No. 103345.
(35) Lanin, A.; Fedik, I.; SpringerLink. *Thermal Stress Resistance of Materials*, 1st ed.; Springer Berlin Heidelberg: Imprint: Springer: Berlin, Heidelberg, 2008.
(36) Barron, R. F.; Barron, B. R.; Knovel. *Design for thermal stresses*; Wiley: Hoboken, NJ, 2012.
(37) Wang, C. H.; Cheng, Y. P.; He, X. X.; Yi, M. H.; Wang, Z. Y. Size effect on uniaxial compressive strength of single coal particle under different failure conditions. *Powder Technol.* **2019**, *345*, 169−181.

https://doi.org/10.1021/acsomega.2c05849
ACS Omega 2022, 7, 44298−44309